Tungsten (2023) 5:288–299
https://doi.org/10.1007/s42864-022-00140-x

Tungsten
www.springer.com/42864

REVIEW PAPER

Visualization of ferromagnetic domains in vanadium-doped topological insulator thin films and heterostructures

Ying-Jie Ma[1] · Ti-Rui Xia[1] · Wen-Bo Wang[1,2]

Received: 12 December 2021 / Revised: 9 January 2022 / Accepted: 10 January 2022 / Published online: 21 February 2022

Abstract

Magnetically doped topological insulator (TI) thin films and related heterostructures have been extensively studied for years due to their exotic quantum transport properties and potential applications in low-dissipation electronic devices and quantum computation. The selection of magnetic dopants is crucial to realize a high-quality magnetic TI with a robust ferromagnetic ordering and a preserved topological band structure. In this paper, we briefly review the recent magnetic domain imaging works in vanadium-doped magnetic topological insulator thin films and heterostructures. Using cryogenic magnetic force microscopy and in situ transport measurements, a ferromagnetic domain behavior has been demonstrated in V-doped Sb_2Te_3 (ST) and Cr, V co-doped $(Bi,Sb)_2Te_3$ (BST) thin films. The direct visualization of long-range ferromagnetic ordering in a quantum anomalous Hall (QAH) system sheds light on enhancing the QAH temperature by improving the ferromagnetism. Taking advantage of the different coercivity of Cr- and V-doped BST films, an axion insulating state has been observed in Cr-doped BST/BST/V-doped BST sandwich heterostructures. The antiparallel magnetization alignment, which is the key ingredient for realization of axion insulating state, has been directly visualized via magnetic imaging at various magnetic fields. The V-doped ST/ST heterostructures also provide a platform for Berry phase engineering in momentum space. By suppressing the anomalous Hall effect in such heterostructures, an intrinsic topological Hall effect can be revealed, which resolved the long-term puzzle of the origin of THE in the ultrathin ferromagnetic thin films and two-dimensional ferromagnets. The review of magnetic domain imaging in vanadium-doped topological insulators and heterostructures inspires further exploration of quantum transport properties in magnetic topological insulators and deepens the understanding of the interplay between the magnetic ordering and topological electronic band structures in magnetic TIs and beyond.

Keywords Vanadium-doped topological insulator · Magnetic force microscopy · Ferromagnetic domain · Quantum anomalous Hall effect · Topological Hall effect

1 Introduction

Topological materials are new states of quantum matter, which possess topological electronic band structures. Breaking time-reversal symmetry in topological materials leads to a variety of quantum phenomena including quantum anomalous Hall effect [1–4], axion insulating state [5–11], Weyl fermions [12–14], Majorana fermions [15, 16] and so on. These exotic quantum phenomena play a crucial role in dissipationless conduction and quantum computation, which stimulates the next industrial revolution. Doping magnetic elements in topological insulators (TIs) might induce ferromagnetism, which opens exchange mass gap at time reversal symmetry protected Dirac point [17–21]. Tuning the Fermi level into the gap leads to dissipationless chiral edge states and zero-field quantized Hall resistance, which are well known as quantum anomalous Hall effect (QAHE). QAHE was first experimentally realized in thin-film specimens of Cr-doped $(Bi,Sb)_2Te_3$(BST) [2–4] and later confirmed in vanadium (V)-doped BST with higher precision of quantum Hall resistance [22]. Compared to chromium, vanadium provides stronger perpendicular magnetic anisotropy (PMA) K and has weaker magnetic moments (~ 1.5 μ_B), which leads to a much larger coercive field (H_C), as the intrinsic H_C is proportional to K/M_S. A large H_C is critical for QAHE, because

✉ Wen-Bo Wang
wangwb1@shanghaitech.edu.cn

[1] School of Physical Science and Technology, ShanghaiTech University, Shanghai 201210, China

[2] ShanghaiTech Laboratory for Topological Physics, ShanghaiTech University, Shanghai 201210, China

it guarantees the single domain state at zero magnetic fields. Vanadium doping also provides stronger exchange coupling (higher T_C) compared with Cr-doped TI films. The higher Curie temperature is favorable to realize QAHE at higher temperatures. In addition, the V-doped ST/ST heterostructures can be utilized as an excellent platform for studying topological Hall effect (THE). Due to their unique band structures, the anomalous Hall effect (AHE) can be tuned to zero at all temperatures, revealing the intrinsic THE [23, 24]. Because of the robust quantum Hall states and controllable momentum-space Berry phase, vanadium-doped topological insulating thin films and heterostructures are widely utilized in quantum electronic devices.

The topological properties of these magnetic topological thin film systems have been extensively studied via quantum transport measurements and angle-resolved photoemission electron spectroscopy (ARPES) measurements [25, 26]. Nevertheless, it is rather challenging to directly probe the magnetic properties of these diluted magnetic semiconductor (DMS) thin films, because of the weak magnetic moments. The signals of bulk magnetic measurements, such as superconducting quantum interference device (SQUID), are usually dominated by the magnetic susceptibility of the substrates. In contrast, magnetic imaging techniques with high sensitivity, which accurately detect local variation of the magnetic moments, are more suitable to study the magnetic properties of this class of materials. Previous scanning SQUID studies of Cr-doped BST films have shown superparamagnetic behavior, which explains the extremely low QAH temperature in these systems [27, 28]. However, scanning SQUID technique only works at low temperatures and weak magnetic fields to maintain the superconducting state of the SQUID tip. Magnetic force microscopy (MFM), which works in a wide range of temperatures and magnetic fields, is another powerful tool to systematically study the local magnetic structures in magnetic TI films. On one hand, the shape of *M-H* hysteresis loops can be obtained by estimating the up and down domain distributions. On the other hand, magnetic inhomogeneity and domain structures, which have a great impact on the topological quantum phenomena, can be directly visualized and correlated with topological properties. Therefore, it is necessary to briefly review the recent progress on MFM studies on vanadium-doped topological insulating thin films and heterostructures, which motivates this short review.

In this review paper, we discuss MFM studies of a variety of vanadium-doped topological insulating thin films and heterostructures, including V-doped ST [29], Cr, V co-doped BST [30], Cr-doped BST/BST/V-doped BST sandwich heterostructure [11] and V-doped ST/ST heterostructure [24, 31]. The interplay between the magnetic properties and topological effects, such as quantum anomalous Hall effect and topological Hall effect, will be explored.

2 Growth of vanadium-doped Sb_2Te_3 thin films

The crystal structure of Sb_2Te_3 is of the tetradymite type [32–34]. It is formed by stacking quintuple-layer groups which consist of three sheets of Te and two sheets of Sb with ABCAB stacking sequence, as shown in Fig. 1a. Vanadium atoms are doped into the structure by replacing the Sb atoms at 2B or 4A sites [35]. The thin films of V-doped Sb_2Te_3 can be grown on various substrates such as Si (111), $SrTiO_3$ and sapphire (0001), using an ultrahigh vacuum molecular beam

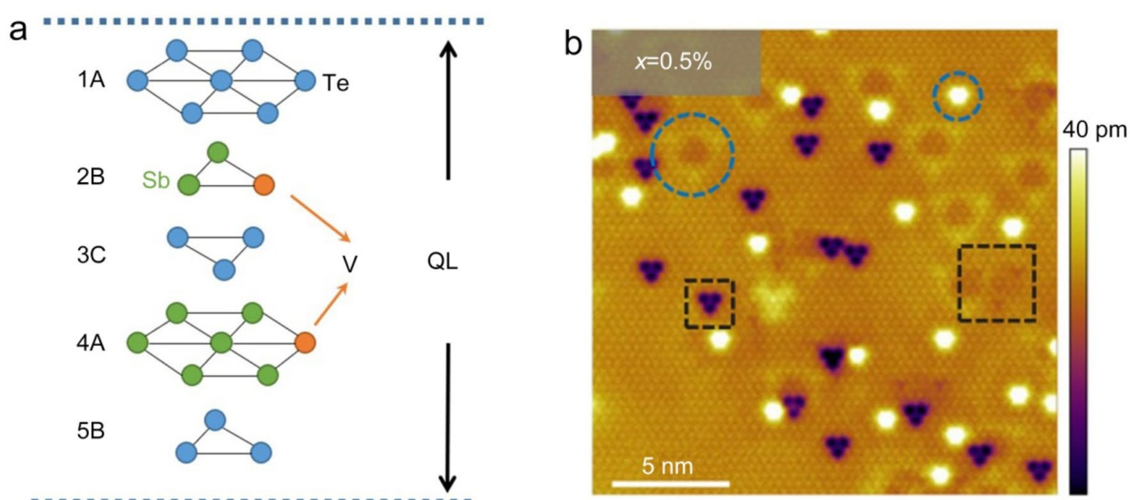

Fig. 1 **a** Crystal structure of one QL of V-doped Sb_2Te_3. **b** STM topographic image of V-doped Sb_2Te_3. Black squares label V_{Sb} defects. Blue circles label Sb_{Te} defects. Reproduced with permission from Ref. [35] Copyright 2018 American Physical Society (APS)

epitaxy (MBE) system [22, 29, 35]. These substrates were heat treated prior to the film growth. High-purity Sb, Te and V elements were evaporated from effusion cells. To avoid Te deficiency, the flux ratio of Te/Sb was set to be ~ 8. The Sb and V concentrations depend on their nominal ratio, which can be in situ monitored during film growth via quartz crystals. The growth rate was controlled ~ 0.2 QL/min for high-quality films. Scanning probe microscopy (STM) studies were performed on V-doped Sb_2Te_3 films. Figure 1b shows a representative topographic image [32]. V dopants presumably replace Sb atoms, leading to V_{Sb} defects at 4A or 2B sites, as labeled by black boxes. Due to different depths, the V_{Sb} defects at 4A sites are represented by large light-colored triangles with slightly darkened centers and corners, whereas those at 2B sites are represented by smaller dark triangles. Sb_{Te} antisite can be also visualized in STM images, which is labeled by blue circles in Fig. 1b.

3 Ferromagnetic domains in vanadium-doped Sb_2Te_3 thin films

V-doped BST film is the second magnetic TI system that exhibits QAHE [22]. Compared to Cr-doped BST films, V-doped ones have a more robust QAH state, with higher precision. Moreover, V-doped BST film is a hard ferromagnet with a stronger magnetic coercivity (H_C ~ 1.0 T) and higher ferromagnetic ordering temperature. These magnetic properties make the V-doped BST thin film an ideal platform for magnetic domain imaging. Besides the robust ferromagnetism and QAHE, a mysterious self-magnetization effect was reported in V-doped BST thin films [22]. Finite net magnetization emerges in the virgin state after zero-field cooling, which is not a common phenomenon in traditional ferromagnetic materials. To explain these phenomena, MFM measurements were performed to study the ferromagnetic domain states of V-doped Sb_2Te_3 thin films after different magnetic field cooling processes [29].

Topographic and MFM images of the $Sb_{1.89}V_{0.11}Te_3$ thin film are shown in Fig. 2. The film was zero-field cooled (ZFC) down to 5 K and measured at 5 K, as shown in Fig. 2a,b. In Fig. 2a, the film exhibits a clean surface with roughness of ~ 1.9 nm. The virgin domain states with equal population of up and down domains can be observed from Fig. 2b, unlikely the reported self-magnetization behavior. Figure 2a–g depicts the domain states after field cooling (FC) with different applied magnetic fields. The film was thermally elevated to 60 K without any applied magnetic field and then cooled down to 5 K with the superconducting magnet. The values of applied magnetic fields generated

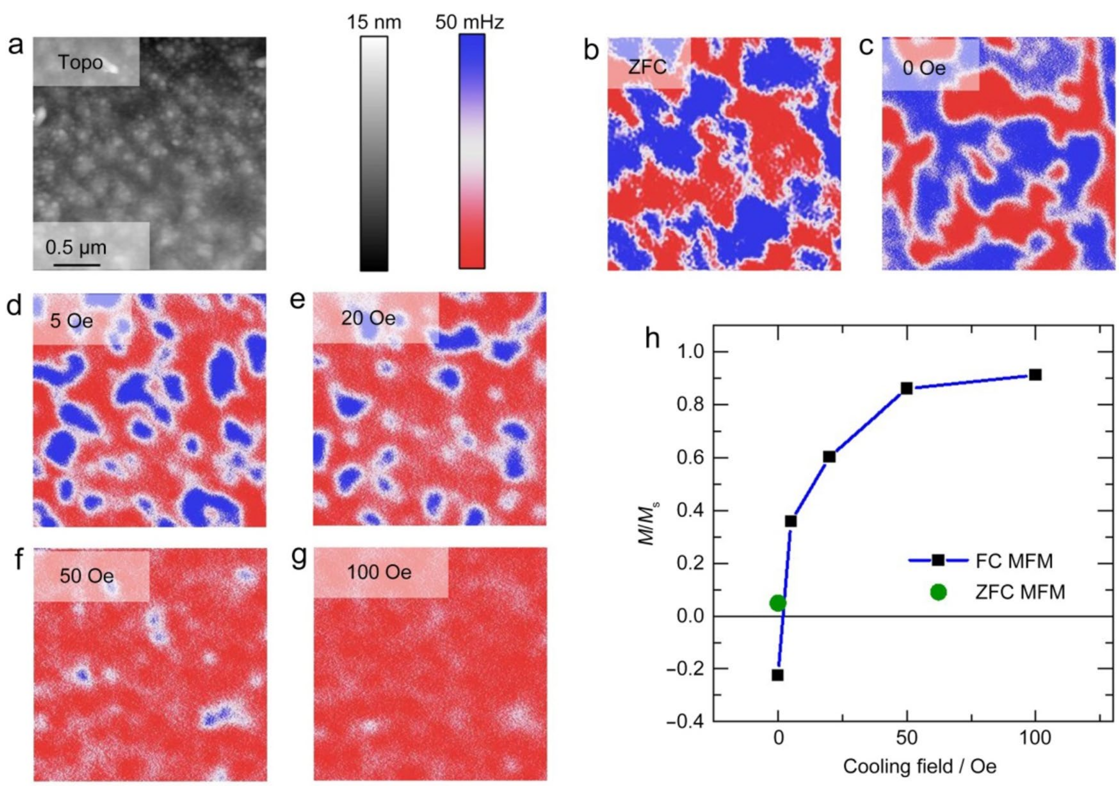

Fig. 2 **a** Topographic and **b–g** MFM images measured on $Sb_{1.89}V_{0.11}Te_3$ thin film at various cooling fields. The nominal cooling fields are labeled at the top left corners. **h** Estimated M/M_S from MFM images after various cooling fields and ZFC

by the superconducting magnet are noted on the upper left side of each picture. Figure 2c shows the film has a slightly negative polarization, due to a trapped magnetic flux in the superconducting magnet when ramping down from a positive value to zero. A weak applied magnetic field of 5 Oe, as shown in Fig. 2d, can significantly polarize the film, and it gets to saturation at 100 Oe, as shown in Fig. 2g. In Fig. 2h, normalized magnetization (magnetization *M*/saturation magnetization M_S) can be estimated by the number of up (N↑) and down (N↓) domains, for example, (N↑ − N↓)/(N↑ + N↓). The normalized magnetization was the function of cooling field in this panel, with the five square points and one circle point just corresponding to Fig. 2c–g and b, respectively. The magnetic flux trapped in the superconducting magnet is estimated to be 3 Oe by linear extrapolation, indicating the reported self-magnetization behavior is likely due to a trapped magnetic flux in the superconducting magnet.

Figure 3 shows field-dependent MFM images of domain states at 5 K after ZFC, indicating the ferromagnetic domain states of the film. The domain states with different values of applied magnetic field at 5 K can be observed from Fig. 3a–l. Higher applied field causes more red (up) domains, and the sample reaches saturation at 1.5 T, as shown in Fig. 3a–f. The film stays in the saturation state at zero field, indicating a strong PMA. Applying negative fields causes magnetization switching of the film, as shown in Fig. 3g–l. The magnetization reversal process from Fig. 3a–l is consistent with typical ferromagnetic reversal behavior. This reversal process is depicted as an *M*–*H* hysteresis loop in Fig. 3m. The panel also shows the butterfly loop of two-probe resistance across the film, highly matching the hysteresis loop. The slight difference of the coercive fields is ascribed to the magnetic tip stray field. The MFM results indicate a hard ferromagnetic behavior with a strong PMA in $Sb_{1.89}V_{0.11}Te_3$

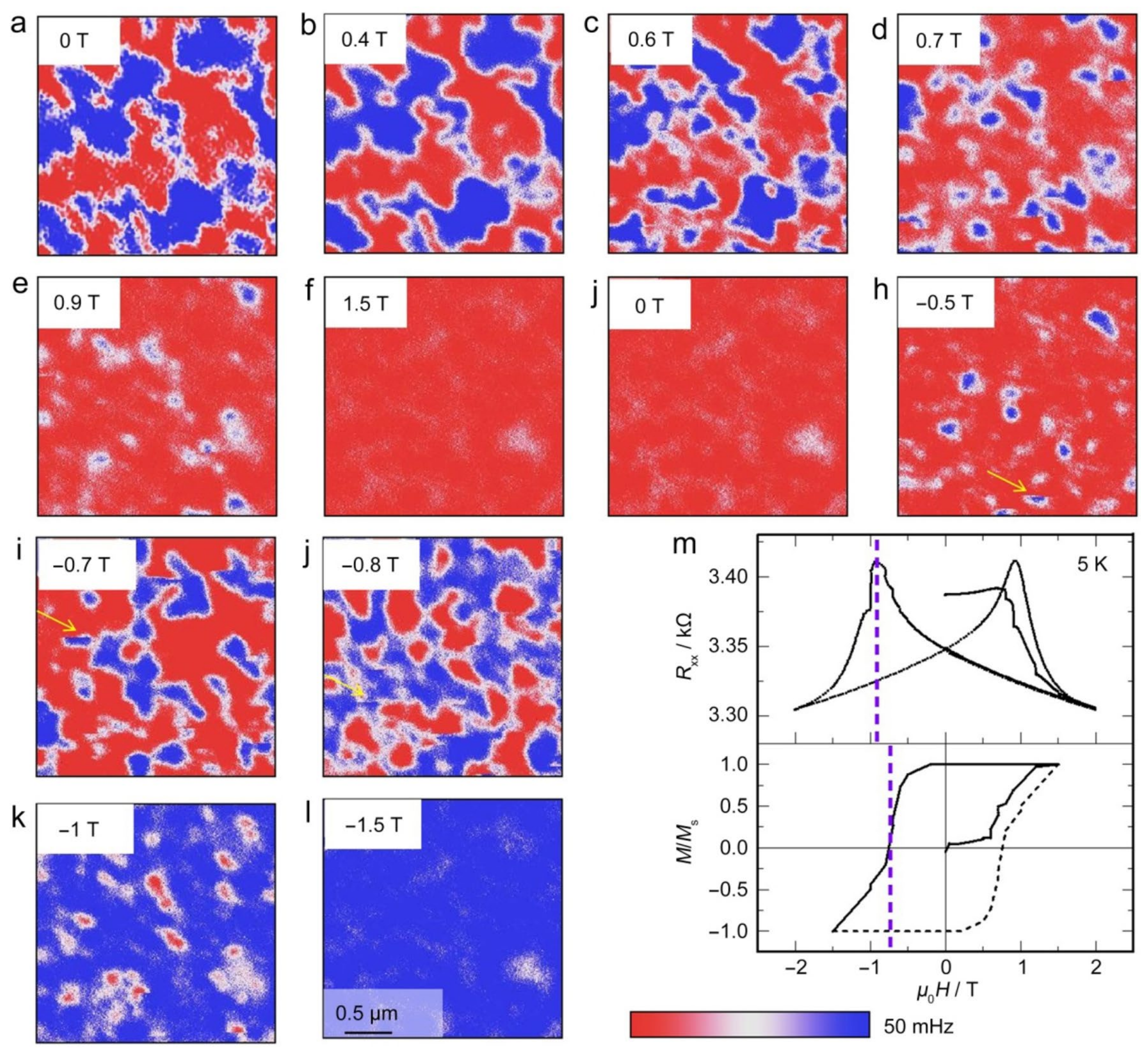

Fig. 3 **a**–**l** 5 K MFM images measured at various magnetic fields from 0 T → 1.5 T → − 1.5 T after ZFC. **m** Longitudinal resistance R_{xx} and estimated M/M_S at various fields. Purple dashed lines represent coercive fields deduced from R_{xx}–*H* and M/M_S–*H* loops

thin film. Compared to Cr-doped TI thin films, which show inhomogeneity and superparamagnetism [27], the V-doped ones are more homogeneous with less disorder.

4 Ferromagnetism in a quantum anomalous Hall system

Although direct evidence of ferromagnetism has been observed in V-doped Sb_2Te_3, this specimen is too conductive to exhibit QAHE. In this section, we will exhibit the direct visualization of ferromagnetism in Cr and V co-doped BST films which shows robust QAHE [30].

The main issue that hinders the further exploration of QAHE in magnetic TIs is the ultralow QAHE temperature. For both Cr- and V-doped BST films, full quantization of Hall resistance was observed below 50 mK [2, 22]. The magnetic inhomogeneity and VBM above the Dirac point may be the two main issues responsible for the ultralow QAH temperature [25, 27, 36–38]. The magnetic inhomogeneity or superparamagnetism generate low magnetic gap regions. Chiral edge states may scatter into bulk and surface states in such regions and destroy the QAH states. However, this is not the only factor that limits the QAH temperature. For instance, the QAH temperature is still low (~ 30 mK) in V-doped TI films, even though the magnetic properties are improved in these systems [22]. Based on ARPES studies, the Dirac point of the surface states is located below the valence band maximum, so that bulks states are introduced when the Fermi level is tuned to the Dirac point for realization of the chiral edge states [25]. It requires extremely low temperature to localize such bulks states to realize full quantization of Hall resistance. Thus, a magnetic TI material with robust ferromagnetic ordering and a 'clean' band structure (Dirac point lies inside the bulk band gap) is necessary to significantly enhance the QAH temperature.

Alloying is a common method to effectively enhance the magnetic properties of metals. Recently, enhanced QAH temperature was achieved in Cr, V co-doped BST thin films [39]. At optimized Cr/V doping ratio, full Hall quantization can be realized at 300 mK, one order of magnitude higher than the singly doped end members [39]. The Hall hysteresis loop shows a sharper magnetization reversal, i.e., less magnetic inhomogeneity. Furthermore, the temperature-dependent anomalous Hall resistance shows a more mean field-like behavior. These pieces of evidence indicate improved ferromagnetism in Cr/V co-doped thin films. However, direct visualization of ferromagnetic domains supporting long-range ferromagnetic ordering is still lacking. Note that intrinsic AHE is governed by the momentum-space Berry phase, which is not directly correlated with magnetization strength [40]. Systematic MFM measurements on these co-doped thin films were performed to confirm the improved ferromagnetism.

Various $(Cr_yV_{1-y})_{0.19}(Bi_xSb_{1-x})_{1.81}Te_3$ films and the Hall bar device were fabricated for MFM and in situ transport measurements, as shown in Fig. 4a. y takes a value between 0 and 1, and $x \approx 0.2$. Figure 4b shows Cr concentration y dependence of Hall conductance σ_{xy} and the ratio of coercivity H_C to $FWHM^{MR}$, which is the full width at half maximum of the magnetoresistance. They were all measured at 1.5 K. The sharpest reversal could be observed at $y = 0.16$, indicating the best ferromagnetic behavior. The maximum of Hall conductance is also at this point. Therefore, the film with the y value of 0.16 is the optimized sample.

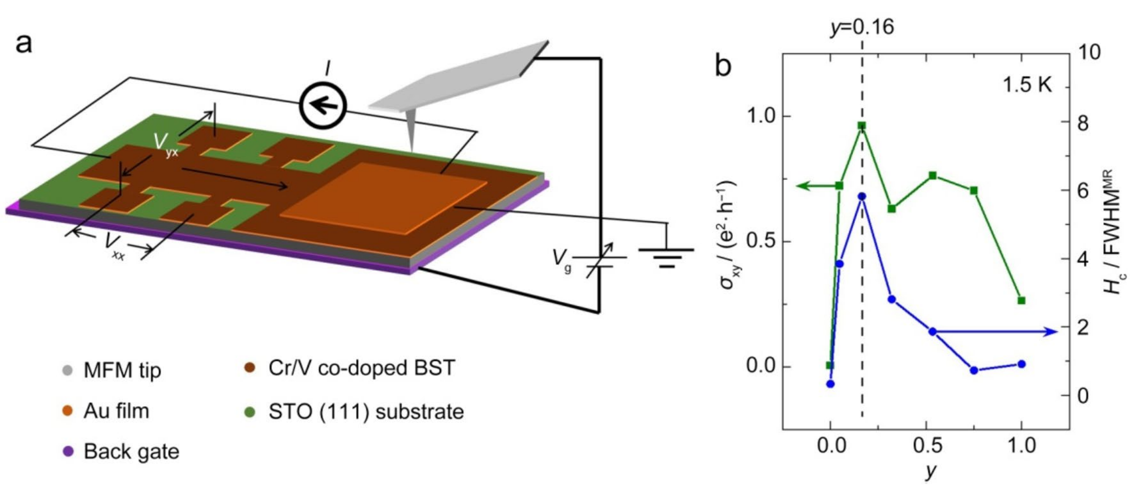

Fig. 4 **a** Hall bar device grown on STO (111) substrate for MFM and in situ transport measurements. A back-gate voltage was applied to tune the charge carrier density. **b** At 1.5 K, Cr concentration (y) dependence of the zero-field Hall conductance (σ_{xy}) and the ratio of coercive field to the full width at half maximum of the magnetoresistance shows a maximum at $y = 0.16$

To verify the improved ferromagnetism in the $y = 0.16$ sample, MFM and in situ transport measurements were taken at 5 K, and the neutral point V_g^0 (≈10 V), as shown in Fig. 5. Figure 5a–i shows the magnetization reversal process with the applied field from 0.05 T to 0.35 T. The sample shows a single-domain state (red) at 0.05 T, suggesting its robust ferromagnetism. The nucleation of up domains (blue) could be observed at 0.15 T, and they expand with increasing fields. The sample gets into an upward saturated state at 0.35 T, as shown in Fig. 5i. The magnetization reversal exhibits a typical ferromagnetic domain behavior via domain nucleation and domain wall propagation. Figure 5j shows field dependence of longitudinal resistance ρ_{xx}, Hall resistance ρ_{yx}, domain contrast δf, and normalized magnetization M/M_S. The normalized magnetization, estimated by the number of up and down domains from MFM data, agrees well with the ρ_{yx} loop. The domain contrast could be represented by the root mean square (rms) value of the MFM data. The peak of it appears at H_C, where up and down domains are equally distributed. At this point, ρ_{xx} also reaches its peak, and $\rho_{yx} = 0$. These are consistent with normalized magnetization, which is equal to zero at H_C. The excellent agreement between local and global results shows great reliability of MFM measurements on the magnetic properties of the sample.

MFM images of the sample at various back-gate voltages were taken to study the ferromagnetism as a function of charge carrier density [31]. The MFM results show larger domains, stronger domain contrast and larger coercive field at $V_g = -300$ V (hole doped), while the situation is opposite at $V_g = 300$ V (electron doped). The ρ_{yx} loops are consistent with the MFM images, which exhibits higher H_C with hole doping and lower with electron doping. The carrier density dependence of ferromagnetism provides compelling evidence of the Ruderman–Kittel–Kasuya–Yosida (RKKY) mechanism. Since the Fermi level is close to the valence band maximum, hole doping can introduce more bulk charge carriers which might enhance the RKKY interaction. Thus, ferromagnetism gets stronger with hole doping. The direct evidence of the ferromagnetism eases the concerns for the absence of long-range magnetic ordering in the QAH systems, which paves the way for realizing QAHE at higher temperatures.

5 Antiparallel magnetization alignment in a quantum anomalous Hall heterostructure for realizing axion insulating states

In a 3D TI, there exist axion term $S_\theta = \frac{\theta}{2\pi}\frac{e^2}{h}\int d^3x dt \boldsymbol{E}\cdot\boldsymbol{B}$ [2–4], the quantized magnetooptical effect [8, 41], the topological magnetoelectric effect (TME) [2–4], and the magnetic monopole [42]. The TME effect is the quantized version of the magnetoelectric effect, i.e., the quantized ME coefficient. The realization of TME requires all the surface

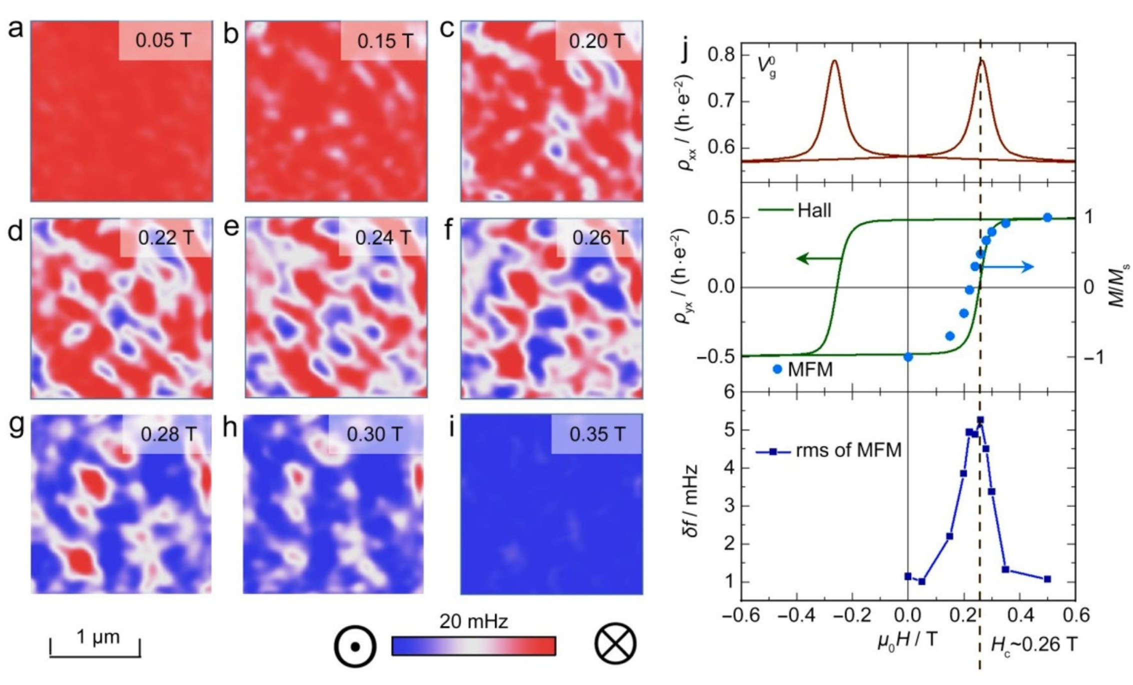

Fig. 5 **a–i** MFM images measured on Cr, V co-doped sample at various magnetic fields at 5 K and V_g^0. **j** ρ_{xx}, ρ_{yx}, M/Ms and δf as a function of magnetic fields. The coercive field Hc≈0.26 K is consistent for these data from transport and MFM measurements

states gapped out. A sandwich heterostructure was proposed to realize the axion insulating states (AIS), where the top and bottom magnetic TI layers have antiparallel magnetization alignment to eliminate the chiral edge modes.

Recently, Mogi et al. [9] and Xiao et al. [11] claimed AIS in the tri-layer heterostructure Cr-doped BST/BST/V-doped BST. Since Cr-doped BST and V-doped BST films have substantially different coercive fields, it is promising to realize the antiparallel magnetization alignment, by controlling the thickness of the spacing TI layer (BST layer) to minimize the interlayer exchange coupling. Although zero Hall resistance plateau has been observed in the heterostructure [11], the direct evidence of the antiparallel magnetization alignment is still lacking. Here, we used the cryogenic MFM system to study the magnetization switching behavior in Cr-doped BST (3 QL)/BST (5 QL)/V-doped BST (3 QL) heterostructures.

Figure 6 shows two-step magnetization switching in sandwich heterostructure at $T = 5.3$ K and $V_g = 0$. MFM images at different applied magnetic fields are shown in Fig. 6a–l. The sample was first swept upward to $\mu_0 H = 1.5$ T and then downward. Figure 6a shows uniformly magnetized (red) domains at $\mu_0 H = -0.01$ T, which means V- and Cr-doped TI layers are both upward magnetized. Cr-doped TI layer gradually switches with increasing applied fields, as shown in Fig. 6c–g. When $\mu_0 H = -0.09$ T, domains changed into green from red, indicating magnetization is entirely switched from up to down in the Cr-doped TI layer. This corresponds to a uniform antiparallel magnetization alignment over the whole heterostructure. Figure 6h–l show magnetization reversal process in the V-doped layer. As Fig. 6l shows, no green domain remains at $\mu_0 H = -0.75$ T, when uniform downward parallel magnetization alignment forms. Figure 6m–o show field dependence of ρ_{yx} (longitudinal resistance), ρ_{yx} (Hall resistance), and δf (magnetic domain contrasts) respectively. Figure 6n shows an obvious two-step transition. As shown in Fig. 6o, two peaks in δf correspond to coercive fields in V- and Cr-doped TI layers, which are in excellent agreement with ρ_{yx} data in Fig. 6n. The direct visualization of antiparallel magnetization alignment in the quantum anomalous Hall heterostructures provides compelling evidence for the realization of AIS.

6 Topological Hall effect in vanadium-doped topological insulator heterostructures

As demonstrated in previous sections, vanadium-doped topological insulators have exotic topological band structures, leading to a fascinating momentum-space Berry phase effect. In this section, we will switch from momentum-space Berry phase phenomena to a real space one, namely the topological Hall effect (THE). The THE originates from scalar spin chirality, which can be represented by the topological charge (TC) Q:

$$Q = \frac{1}{4\pi} \int d^2\boldsymbol{r}\boldsymbol{s} \cdot (\partial_x \boldsymbol{s} \times \partial_y \boldsymbol{s}),$$

where $\boldsymbol{s}$ represents a unit vector that continuously rotates in real space. For two-dimensional spin lattice model, the

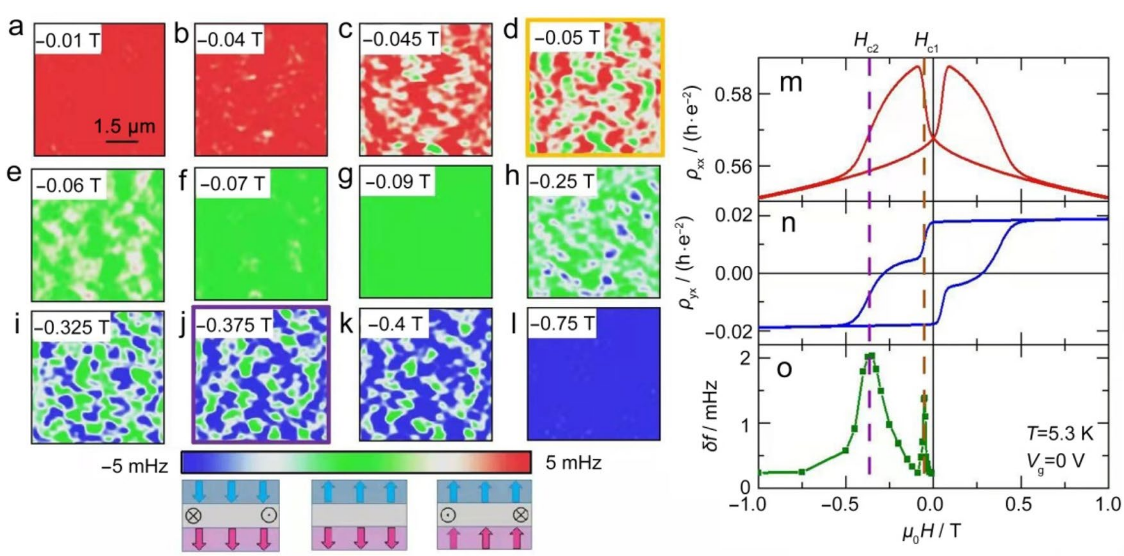

Fig. 6 **a–l** MFM images measured on Cr-doped BST (3 QL)/BST (5 QL)/V-doped BST (3 QL) heterostructure at various magnetic fields at 5.3 K and 0 V. Red and blue regions represent parallel up and down magnetization alignment for QAHE states, while green regions represent antiparallel magnetization alignment for axion insulating states. (m) ρ_{xx}, (n) ρ_{yx} and (o) δf as a function of magnetic fields. H_{c1} and H_{c2} are coercive fields for Cr-doped BST (3 QL) and V-doped BST (3 QL) layers, respectively

total TC can be estimated by the sum of the solid angle Ω subtended by spin triads [43, 44]. As an electron travels through the non-coplanar spin texture, it will experience an effective magnetic field. This field, originating from the Berry phase generated by the electron as it hops between magnetic moments, will in turn give rise to a Hall effect known as the THE. In reality, THE has been demonstrated in many skyrmion systems, e.g., MnSi [44, 45] and FeGe [46]. For a long time, THE is regarded as a hallmark of the formation of static skyrmions. Recently, pronounced THE has been observed in various ferromagnetic ultrathin films, such as Cr-doped $(Bi_{1-x}Sb_x)Te_3$ [47], Mn-doped Bi_2Te_3 [48], CrTe [49], and $SrIrO_3/SrRuO_3$ bilayer structures [50, 51]. The origin of the THE signals in these systems is still under debate. Although the formation of Neel-type skyrmions was claimed in some of these papers, two opposite AHE effects with different coercivity in inhomogeneous films may also generate such Hall signals [52, 53]. Therefore, it is urgent to systematically study the underlying mechanism of THE in two-dimensional (2D) ferromagnets and ultrathin magnetic films.

In general, the total Hall resistivity consists of three contributions in a magnetic conductor: the ordinary Hall effect (OHE) linear with external magnetic field H, the AHE linear with magnetization M, and the THE linear with TCs [44, 46, 54]. Therefore, the Hall resistivity can be written as $\rho_{yx}(H) = \rho_0 H + \rho_A M + \rho_{yx}^T$. The OHE contribution can be deduced from the slope at high magnetic fields. The characterization of AHE, however, requires delicate magnetometry to precisely determine the M–H loop, which could be challenging for some systems. This problem can be circumvented if AHE can be manually suppressed by momentum-space Berry phase engineering. Recently, Wang et al. [23] observed the sign reversal of AHE in m QL Sb_2Te_3/5 QL $Sb_{1.9}V_{0.1}Te_3$ heterostructures. The charge transfer between the ST and VST layers, controlled by the thickness of ST layer, moves the Fermi level of the VST layer closer to band crossing points. A back-gate voltage can be applied to fine-tune the Fermi level across these points, resulting in a sign change of the AHE. In addition, for $m=3$ heterostructure, the AHE can be zeroed via back gating at all temperatures. This makes ST/VST heterostructures an excellent platform to study THE, because the intrinsic THE, if exists, can be directly visualized in these systems.

Figure 7a shows a schematic picture of the VST heterostructure structure for MFM measurements. A VST (5 QLs)/ST (3 QLs) bilayer structure was grown on STO substrates. A thin layer of Pt was coated on the surface of the sample for electric potential balance to eliminate electrostatic interaction. As shown in Fig. 7b, the raw Hall data at 30 K exhibits a positive slope, indicating p-type charge carriers. Here, we focus on the anomalous part: $\tilde{\rho}_{yx} \equiv \rho_{yx} - \rho_0 H$, after the OHE was subtracted out. By applying a back-gate voltage, the $\tilde{\rho}_{yx}$ can be exactly tuned to zero and the intrinsic THE is revealed, as shown in Fig. 7c. The complete THE data at various temperatures between 6 and 40 K are shown in Fig. 8. The temperature dependence of the amplitude of THE signals shows one maximum around Curie temperature ~ 27.5 K. Such antisymmetric AHE peaks without magnetic hysteresis exist above T_C originates from the spin chirality fluctuation. Similar behavior has been observed in $STO/SrRuO_3$ bilayer structures grown on STO substrate [31].

To better understand the emergent spin chirality fluctuation in 2D ferromagnets with PMA, Monte Carlo (MC) simulations were carried out based on the following Hamiltonian:

$$H = \sum_{<ij>}[-J(\boldsymbol{S}_i \cdot \boldsymbol{S}_j) + D_{ij} \cdot (\boldsymbol{S}_i \times \boldsymbol{S}_j)] - K\sum_i (S_i^z)^2 - B_z \sum_i S_i^z,$$

where $\boldsymbol{S}_i$ is the spin on the ith lattice site. The first term $(J>0)$ denotes ferromagnetic Heisenberg exchange

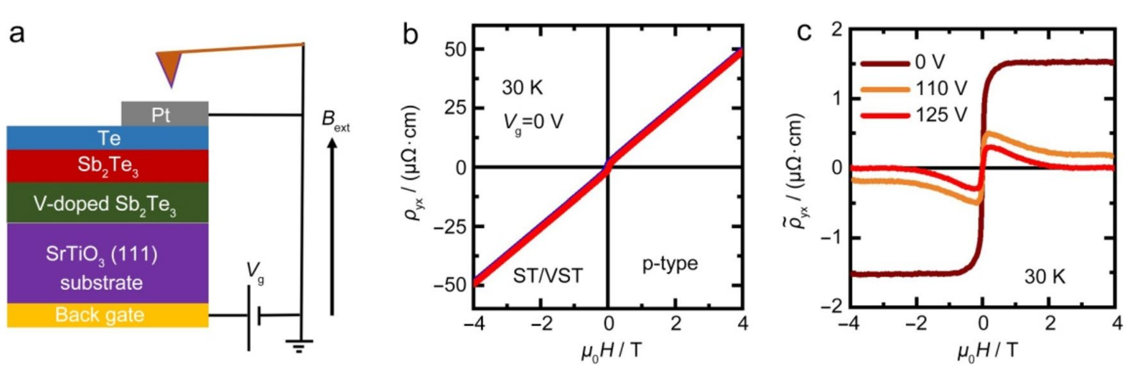

Fig. 7 **a** A schematic of ST/VST heterostructure grown on STO (111) substrate for MFM and in situ transport measurements. A back-gate voltage was applied to tune the AHE. **b** Raw data ρ_{yx} of ST/VST film at 30 K. The positive slope at high fields indicates p-type carriers. **c** $\tilde{\rho}_{yx}$ of VST film at 30 K with different back-gate voltages. The AHE can be tuned to zero at 125 V so that only THE is visible

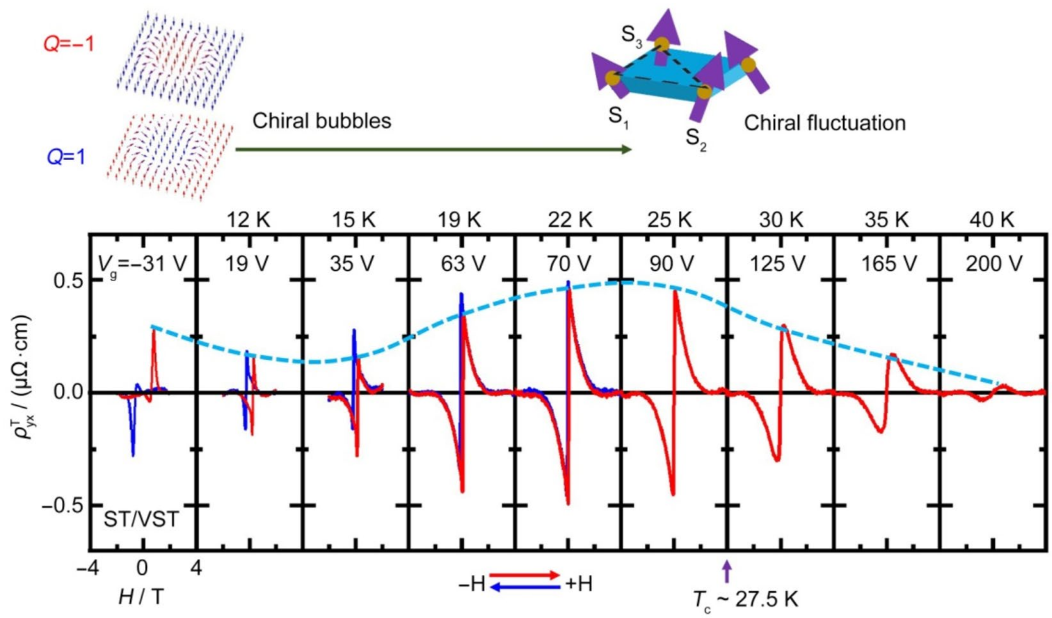

Fig. 8 Intrinsic ρ_{yx}^{T} at various temperatures after AHE is tuned to zero. The low-temperature THE is ascribed to chiral bubbles formed around coercive fields, while the high-temperature THE around $T_{\mathrm{C}} \sim 27.5$ K is ascribed to spin chirality fluctuations

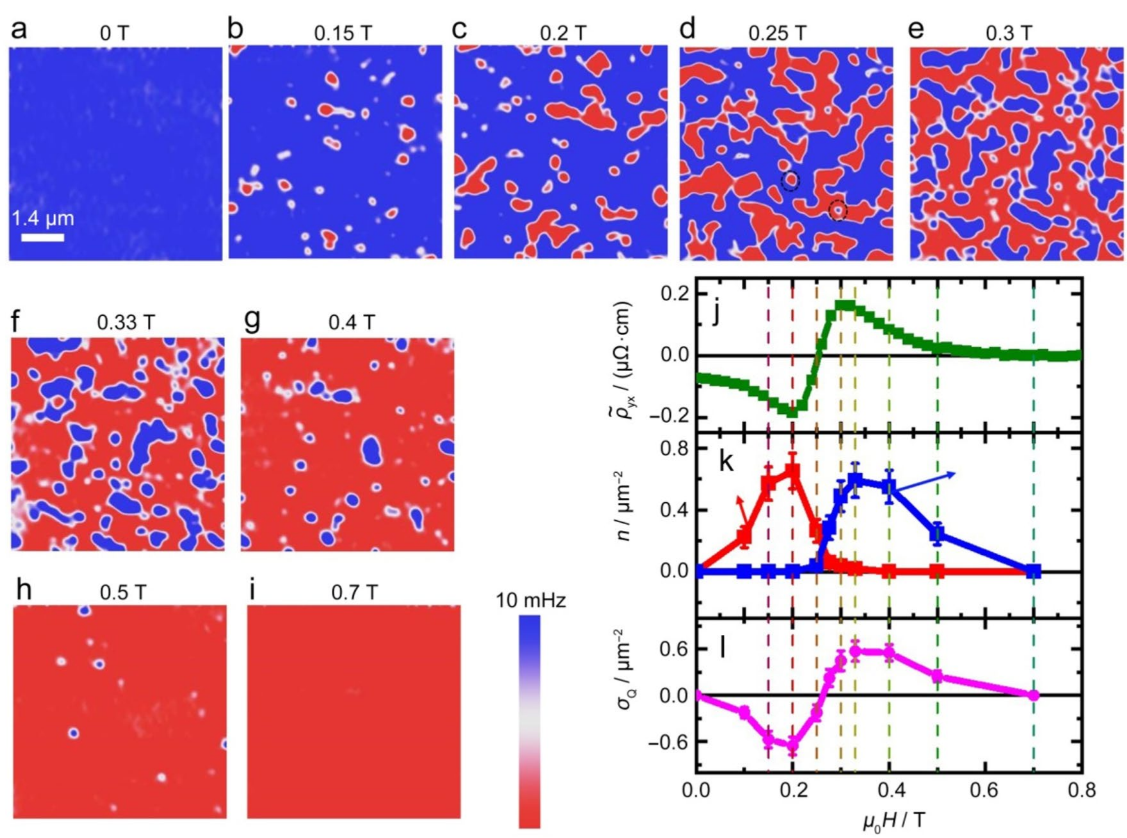

Fig. 9 **a–i** Field-dependent MFM images were measured at $V_{\mathrm{g}} = 19$ V and 12 K. **j** Hall resistivity $\tilde{\rho}_{yx}$ at various magnetic fields. k density (n) of nucleation ($Q = -1$) and pinned ($Q = 1$) bubbles at various magnetic fields, estimated from MFM images. **l** the density (σ_{Q}) of TC at various magnetic fields. The field dependence of σ_{Q} is consistent with the topological Hall resistance (**j**)

interaction. The second term denotes Dzyaloshinsky–Moriya interaction (DMI) [55, 56], due to the inversion symmetry breaking at the interface. The third term represents the uniaxial anisotropy K. When D is smaller than the critical value, the ground state is ferromagnetic with uniform perpendicular magnetization regardless of the existence of DMI [57]. The Zeeman energy due to the external magnetic field is shown in the last term. The MC simulations excellently reproduce the experimentally observed antisymmetric THE peaks, which provides compelling evidence of chiral fluctuation-driven topological responses.

At low temperature ($\ll T_C$), hysteretic THE is revealed around coercive fields, when ferromagnetic domains usually form. Such low-temperature THE is likely correlated with the formation of ferromagnetic domains with determined chirality. To verify this, MFM images and in situ transport measurements are shown in Fig. 9. Magnetization reversal process at 12 K shown in Fig. 9a–i complies with typical ferromagnetic domain behavior via domain nucleation and domain wall propagation [11 29]. During this process, magnetic bubbles with chiral domain walls would form, because of the DMI on the interface. Due to the topological nature of the chiral magnetic bubbles, each bubble carries an integer number of TCs, regardless of its size and shape. Since MFM is incapable of determining the topological charge of each bubble, $Q = \pm 1$ was assigned to each bubble in the MFM images. The number of nucleation bubbles (red) reaches a maximum at 0.2 T, in agreement with the negative THE peak. In addition, the number of pinned bubbles reaches a maximum at 0.3 T, in agreement with the positive THE peak. The nucleation and pinned bubbles have identical chirality but opposite polarization, and therefore carry $Q = -1$ and $Q = 1$ topological charges, respectively [58]. The opposite chiral bubbles are equally distributed at $\mu_0 H_C \approx 0.25$ T, consistent with the absence of THE at the coercive field. Figure 9k plots the density of $Q = -1$ and $Q = 1$ bubbles within the scanned area [59]. The field-dependent net topological charge density (magenta curve) is in great agreement with the in situ THE (green curve), indicating chiral bubble-induced THE. MC simulations and back-gate dependence of MFM data suggest magnetic defects could be the origins of these nucleation and pinned bubbles [24]. These results open a route to control and manipulate TCs via magnetic defect engineering.

7 Conclusion

In conclusion, we briefly review the magnetic domain imaging studies on various vanadium-doped magnetic TI films and heterostructures. MFM imaging technique together with in situ transport measurement is a powerful tool to study magnetic topological materials. The momentum-space and real-space Berry phase effect can be probed via in situ Hall measurements, e.g., QAHE, AIS and THE. Simultaneously, the magnetic domain states can be mapped out via MFM imaging. The relation between the magnetic domain structures and the topological properties therefore can be explored at various temperatures and magnetic fields. Recently, more fascinating magnetic topological materials have be discovered, e.g., intrinsic magnetic TI $MnBi_2Te_4$ [60], twisted bilayer graphene with orbital magnetism [61], magnetic Weyl semimetal EuB_6 [14] and so on. The exploration of the interplay between magnetism and topology in these materials is fundamentally interesting to condensed matter physicists and will be crucial for realizing the exotic topological states at a higher temperature, which can be practically utilized in dissipationless electronic devices and quantum computation.

Acknowledgements This work was financially supported by the starting grant of ShanghaiTech University. W.W. acknowledges the support from Science and Technology Commission of Shanghai Municipality (Grant No. 21PJ410800).

Declarations

Conflict of interest The authors state that there are no conflict of interest to disclose.

References

1. Haldane FDM. Model for a quantum Hall effect without landau levels: condensed-matter realization of the “parity anomaly.” Phys Rev Lett. 1988;61(18):2015.
2. Chang CZ, Zhang JS, Feng X, Shen J, Zhang ZC, Guo MH, Li K, Ou YB, Wei P, Wang LL, Ji ZQ, Feng Y, Ji SH, Chen X, Jia JF, Dai X, Fang Z, Zhang SC, He K, Wang YY, Lu L, Ma XC, Xue QK. Experimental observation of the quantum anomalous Hall effect in a magnetic topological insulator. Science. 2013;340(6129):167.
3. Checkelsky JG, Yoshimi R, Tsukazaki A, Takahashi KS, Kozuka Y, Falson J, Kawasaki M, Tokura Y. Trajectory of the anomalous Hall effect towards the quantized state in a ferromagnetic topological insulator. Nat Phys. 2014;10:731.
4. Kou X, Guo ST, Fan Y, Pan L, Lang M, Jiang Y, Shao Q, Nie T, Murata K, Tang J, Wang Y, He L, Lee TK, Lee WL, Wang KL. Scale-invariant quantum anomalous Hall effect in magnetic topological insulators beyond the two-dimensional limit. Phys Rev Lett. 2014;113:137201.
5. Qi XL, Hughes TL, Zhang SC. Topological field theory of time-reversal invariant insulators. Phys Rev B. 2008;78(19):195424.
6. Wang J, Lian B, Qi XL, Zhang SC. Quantized topological magnetoelectric effect of the zero-plateau quantum anomalous Hall state. Phys Rev B. 2015;92(8):081107.
7. Morimoto T, Furusaki A, Nagaosa N. Topological magnetoelectric effects in thin films of topological insulators. Phys Rev B. 2015;92(8):085113.
8. Wu L, Salehi M, Koirala N, Moon J, Oh S, Armitage NP. Quantized Faraday and Kerr rotation and axion electrodynamics of a 3D topological insulator. Science. 2016;354(6316):1124.
9. Mogi M, Kawamura M, Tsukazaki A, Yoshimi R, Takahashi KS, Kawasaki M, Tokura Y. Tailoring tricolor structure of

magnetic topological insulator for robust axion insulator. Sci Adv. 2017;3:1669.

10. Mogi M, Kawamura M, Yoshimi R, Tsukazaki A, Kozuka Y, Shirakawa N, Takahashi KS, Kawasaki M, Tokura Y. A magnetic heterostructure of topological insulators as a candidate for an axion insulator. Nat Mater. 2017;16(5):516.
11. Xiao D, Jiang J, Shin JH, Wang W, Wang F, Zhao YF, Liu C, Wu W, Chan MHW, Samarth N, Chang CZ. Realization of the axion insulator state in quantum anomalous hall sandwich heterostructures. Phys Rev Lett. 2018;120(5):56801.
12. Liu DF, Liang AJ, Liu EK, Xu QN, Li YW, Chen C, Pei D, Shi WJ, Mo SK, Dudin P, Kim T, Cacho C, Li G, Sun Y, Yang LX, Liu ZK, Parkin SSP, Felser C, Chen YL. Magnetic Weyl semimetal phase in a Kagome crystal. Science. 2019;365(6459):1282.
13. Morali N, Batabyal R, Nag PK, Liu E, Xu Q, Sun Y, Yan B, Felser C, Avraham N, Beidenkopf H. Fermi-arc diversity on surface terminations of the magnetic Weyl semimetal $Co_3Sn_2S_2$. Science. 2019;365(6459):1286.
14. Nie S, Sun Y, Prinz FB, Wang Z, Weng H, Fang Z, Dai X. Magnetic semimetals and quantized anomalous Hall effect in EuB_6. Phys Rev Lett. 2020;124(7):076403.
15. Nadj-Perge S, Drozdov IK, Li J, Chen H, Jeon S, Seo J, MacDonald AH, Bernevig BA, Yazdani A. Observation of Majorana fermions in ferromagnetic atomic chains on a superconductor. Science. 2014;346(6209):602.
16. Wang J, Zhou Q, Lian B, Zhang SC. Chiral topological superconductor and half-integer conductance plateau from quantum anomalous Hall plateau transition. Phys Rev B. 2015;92(6):064520.
17. Hor YS, Roushan P, Beidenkopf H, Seo J, Qu D, Checkelsky JG, Wray LA, Hsieh D, Xia Y, Xu SY, Qian D, Hasan MZ, Ong NP, Yazdani A, Cava RJ. Development of ferromagnetism in the doped topological insulator $Bi_{2-x}Mn_xTe_3$. Phys Rev B. 2010;81(19):195203.
18. Dyck JS, Drasar C, Lostak P, Uher C. Low-temperature ferromagnetic properties of the diluted magnetic semiconductor $Sb_{2-x}Cr_xTe_3$. Phys Rev B. 2005;71(11):115214.
19. Zhou Z, Chien YJ, Uher C. Thin film dilute ferromagnetic semiconductors $Sb_{2-x}Cr_xTe_3$ with a Curie temperature up to 190 K. Phys Rev B. 2006;74:224418.
20. Dyck JS, Hajek P, Lostak P, Uher C. Diluted magnetic semiconductors based on $Sb_{2-x}V_xTe_3(0.01\leq_x\leq 0.03)$. Phys Rev B. 2002;65:115212.
21. Haazen PPJ, Laloe JB, Nummy TJ, Swagten HJM, Jarillo-Herrero P, Heiman D, Moodera JS. Ferromagnetism in thin-film Cr-doped topological insulator Bi_2Se_3. Appl Phys Lett. 2012;2015(100):082404.
22. Chang CZ, Zhao W, Kim DY, Zhang H, Assaf BA, Heiman D, Zhang SC, Liu C, Chan MHW, Moodera JS. High-precision realization of robust quantum anomalous Hall state in a hard ferromagnetic topological insulator. Nat Mater. 2015;14:473.
23. Wang F, Wang X, Zhao YF, Xiao D, Zhou LJ, Liu W, Zhang Z, Zhao W, Chan MHW, Samarth N, Liu C, Zhang H, Chang CZ. Interface-induced sign reversal of the anomalous Hall effect in magnetic topological insulator heterostructures. Nat Commun. 2021;12:79.
24. Wang W, Zhao YF, Wang F, Daniels MW, Chang CZ, Zang J, Xiao D, Wu W. Chiral-bubble-induced topological Hall effect in ferromagnetic topological insulator heterostructures. Nano Lett. 2021;21(2):1108.
25. Li W, Claassen M, Chang CZ, Moritz B, Jia T, Zhang C, Rebec S, Lee JJ, Hashimoto M, Lu DH, Moore RG, Moodera JS, Devereaux TP, Shen ZX. Origin of the low critical observing temperature of the quantum anomalous Hall effect in V-doped $(Bi, Sb)_2Te_3$ film. Sci Rep. 2016;6:32732.
26. Ye M, Li W, Zhu S, Takeda Y, Saitoh Y, Wang J, Pan H, Nurmamat M, Sumida K, Ji F, Liu Z, Yang H, Liu Z, Shen D, Kimura A, Qiao S, Xie X. Carrier-mediated ferromagnetism in the magnetic topological insulator Cr-doped $(Sb, Bi)_2Te_3$. Nat Commun. 2015;6:8913.
27. Lachman EO, Young AF, Richardella A, Cuppens J, Naren HR, Anahory Y, Meltzer AY, Kandala A, Kempinger S, Myasoedov Y, Huber ME, Samarth N, Zeldov E. Visualization of superparamagnetic dynamics in magnetic topological insulators. Sci Adv. 2015;1(10):1500740.
28. Lachman EO, Mogi M, Sarkar J, Uri A, Bagani K, Anahory Y, Myasoedov Y, Huber ME, Tsukazaki A, Kawasaki M, Tokura Y, Zeldov E. Observation of superparamagnetism in coexistence with quantum anomalous Hall C=±1 and C=0 Chern states. npj Quantum Mater. 2017;2:70.
29. Wang W, Chang CZ, Moodera JS, Wu W. Visualizing ferromagnetic domain behavior of magnetic topological insulator thin films. npj Quantum Mater. 2016;1(1):16023.
30. Wang W, Ou Y, Liu C, Wang Y, He K, Xue QK, Wu W. Direct evidence of ferromagnetism in a quantum anomalous Hall system. Nat Phys. 2018;14:791.
31. Wang W, Daniels MW, Liao Z, Zhao Y, Wang J, Koster G, Rijnders G, Chang CZ, Xiao D, Wu W. Spin chirality fluctuation in two-dimensional ferromagnets with perpendicular magnetic anisotropy. Nat Mater. 2019;18(10):1054.
32. Chen YL, Analytis JG, Chu JH, Liu ZK, Mo SK, Qi XL, Zhang HJ, Lu DH, Dai X, Fang Z, Zhang SC, Fisher IR, Hussain Z, Shen ZX. Experimental realization of a three-dimensional topological insulator Bi_2Te_3. Science. 2009;325:178.
33. Zhang H, Liu CX, Qi XL, Dai X, Fang Z, Zhang SC. Topological insulators in Bi_2Se_3, Bi_2Te_3 and Sb_2Te_3 with a single Dirac cone on the surface. Nat Phys. 2009;5(6):438.
34. Hsieh D, Xia Y, Qian D, Wray L, Meier F, Dil JH, Osterwalder J, Patthey L, Fedorov AV, Lin H, Bansil A, Grauer D, Hor YS, Cava RJ, Hasan MZ. Observation of time-reversal-protected single-dirac-cone topological-insulator states in Bi_2Te_3 and Sb_2Te_3. Phys Rev Lett. 2009;103(14):2.
35. Zhang W, West D, Lee SH, Qiu Y, Chang CZ, Moodera JS, Hor YS, Zhang S, Wu W. Electronic fingerprints of Cr and V dopants in the topological insulator Sb_2Te_3. Phys Rev B. 2018;98(11):115165.
36. Chang CZ, Tang P, Wang YL, Feng X, Li K, Zhang Z, Wang Y, Wang LL, Chen X, Liu C, Duan W, He K, Ma XC, Xue QK. Chemical-potential-dependent gap opening at the Dirac surface states of Bi_2Se_3 induced by aggregated substitutional Cr atoms. Phys Rev Lett. 2014;112:056801.
37. Lee I, Kim CK, Lee J, Billinge SJL, Zhong RD, Schneeloch JA, Liu TS, Valla T, Tranquada JM, Gu GD, Davis JCS. Imaging Dirac-mass disorder from magnetic dopant atoms in the ferromagnetic topological insulator $Cr_x(Bi_{0.1}Sb_{0.9})_{2-x}Te_3$. Proc Natl Acad Sci U S A. 2015;112(5):1316.
38. Grauer S, Schreyeck S, Winnerlein M, Brunner K, Gould C, Molenkamp LW. Coincidence of superparamagnetism and perfect quantization in the quantum anomalous Hall state. Phys Rev B. 2015;92(20):201304.
39. Ou Y, Liu C, Jiang G, Feng Y, Zhao D, Wu W, Wang XX, Li W, Song C, Wang LL, Wang W, Wu W, Wang Y, He K, Ma XC, Xue QK. Enhancing the quantum anomalous Hall effect by magnetic codoping in a topological insulator. Adv Mater. 2017;30:1703062.
40. Nagaosa N, Sinova J, Onoda S, MacDonald AH, Ong NP. Anomalous Hall effect. Rev Mod Phys. 2010;82(2):1539.
41. Tse WK, MacDonald AH. Giant magneto-optical Kerr effect and universal Faraday effect in thin-film topological insulators. Phys Rev Lett. 2010;105(5):057401.
42. Qi XL, Li R, Zang J, Zhang SC. Inducing a magnetic monopole with topological surface states. Science. 2009;323:1184.

43. Taguchi Y, Oohara Y, Yoshizawa H, Nagaosa N, Tokura Y. Spin chirality, Berry phase, and anomalous Hall effect in a frustrated ferromagnet. Science. 2001;291(5513):2573.
44. Neubauer A, Pfleiderer C, Binz B, Rosch A, Ritz R, Niklowitz PG, Boni P. Topological hall effect in the A phase of MnSi. Phys Rev Lett. 2009;102(18):186602.
45. Li Y, Kanazawa N, Yu XZ, Tsukazaki A, Kawasaki M, Ichikawa M, Jin XF, Kagawa F, Tokura Y. Robust formation of skyrmions and topological Hall effect anomaly in epitaxial thin films of MnSi. Phys Rev Lett. 2013;110(11):117202.
46. Huang SX, Chien CL. Extended skyrmion phase in epitaxial FeGe (111) thin films. Phys Rev Lett. 2012;108(26):267201.
47. Yasuda K, Wakatsuki R, Morimoto T, Yoshimi R, Tsukazaki A, Takahashi KS, Ezawa M, Kawasaki M, Nagaosa N, Tokura Y. Geometric Hall effects in topological insulator heterostructures. Nat Phys. 2016;12(6):555.
48. Liu C, Zang YY, Ruan W, Gong Y, He K, Ma XC, Xue QK, Wang YY. Dimensional crossover-induced topological Hall effect in a magnetic topological insulator. Phys Rev Lett. 2017;119(17):176809.
49. Zhao D, Zhang L, Malik IA, Liao M, Cui W, Cai X, Zheng C, Li L, Hu X, Zhang D, Zhang J, Chen X, Jiang W, Xue Q. Observation of unconventional anomalous Hall effect in epitaxial CrTe thin films. Nano Res. 2018;11(6):3116.
50. Matsuno J, Ogawa N, Yasuda K, Kagawa F, Koshibae W, Nagaosa N, Tokura Y, Kawasaki M. Interface-driven topological Hall effect in $SrRuO_3$-$SrIrO_3$ bilayer. Science Adv. 2016;2(7):1600304.
51. Ohuchi Y, Matsuno J, Ogawa N, Kozuka Y, Uchida M, Tokura Y, Kawasaki M. Electric-field control of anomalous and topological Hall effects in oxide bilayer thin films. Nat Commun. 2018;9(1):213.
52. Kan D, Moriyama T, Kobayashi K, Shimakawa Y. Alternative to the topological interpretation of the transverse resistivity anomalies in $SrRuO_3$. Phys Rev B. 2018;98(18):180408.
53. Kimbell G, Sass PM, Woltjes B, Ko EK, Noh TW, Wu W, Robinson JWA. Two-channel anomalous Hall effect in $SrRuO_3$. Phys Rev Mater. 2020;4(5):054414.
54. Kanazawa N, Onose Y, Arima T, Okuyama D, Ohoyama K, Wakimoto S, Kakurai K, Ishiwata S, Tokura Y. Large topological hall effect in a short-period helimagnet MnGe. Phys Rev Lett. 2011;106(15):156603.
55. Dzyaloshinsky I. A thermodynamic theory of “weak” ferromagnetism of antiferromagnetics. J Phys Chem Solids. 1958;4(4):241.
56. Moriya T. Anisotropic superexchange interaction and weak ferromagnetism. Phys Rev. 1949;1960(120):91.
57. Rohart S, Thiaville A. Skyrmion confinement in ultrathin film nanostructures in the presence of Dzyaloshinskii-Moriya interaction. Phys Rev B. 2013;88:184422.
58. Nagaosa N, Tokura Y. Topological properties and dynamics of magnetic skyrmions. Nat Nanotechnol. 2013;8(12):899.
59. Vistoli L, Wang WB, Sander A, Zhu QX, Casals B, Cichelero R, Barthelemy A, Fusil S, Herranz G, Valencia S, Abrudan R, Weschke E, Nakazawa K, Kohno H, Santamaria J, Wu WD, Garcia V, Bibes M. Giant topological Hall effect in correlated oxide thin films. Nat Phys. 2019;15(1):67.
60. Deng Y, Yu Y, Shi MZ, Guo Z, Xu Z, Wang J, Chen XH, Zhang Y. Quantum anomalous Hall effect in intrinsic magnetic topological insulator $MnBi_2Te_4$. Science. 2020;367(6480):895.
61. Serlin M, Tschirhart CL, Polshyn H, Zhang Y, Zhu J, Watanabe K, Taniguchi T, Balents L, Young AF. Intrinsic quantized anomalous Hall effect in a moire heterostructure. Science. 2020;367(6480):900.